Pergamon

Int. J. Heat Mass Transfer. Vol. 37, No. 12, pp. 1733–1748, 1994

0017-9310/94 $7.00+0.00

0017-9310(93)E0125-Z

Thermocapillary convection and melt–solid interface in the floating zone

J.-C. CHEN, C.-F. CHU and W.-F. UENG

Department of Mechanical Engineering, National Central University, Chung-Li, Taiwan 32054, R.O.C.

(*Received* 21 *September* 1993 *and in final form* 26 *November* 1993)

Abstract—A series of numerical computations is used to study both the amount of power required to form a molten zone and the fluid flow inside the melt. The Navier–Stokes equations and energy equation are solved by a finite difference method, employing a boundary-fitted curvilinear coordinate system. The influences considered include: the magnitude of the input power, the width of the heated region, the fluid properties in the melt, and the heat-transfer condition of the ambient on the solid–melt interface. The present results show that the height of the molten zone increases significantly as the strength of the thermocapillary convection increases. For small Prandtl number fluids, when the input power increases, thermocapillary-flow instability in the melt may appear before the capillary instability (originating from the gas–melt interface) sets in. For higher Prandtl number fluids, the appearance of the capillary instability is more likely than thermocapillary-flow instability. The appearance of thermocapillary-flow instability may be also influenced by the ratio of the surface tension to the viscous force in the melt, the width of the heated region, and the heat loss to the ambient.

1. INTRODUCTION

IN RECENT years the float-zone crystal growth method has been widely used to grow high-purity single crystals because it precludes contamination and thermal stress resulting from the presence of a crucible. In practice, the size of the melt is limited by the capillary instability originating at the meniscus, while the shape of the solid–melt interface and the flow state present in the melt can significantly affect the quality of the resultant crystals.

Thermocapillary flow, which is driven by temperature-induced surface-tension gradients along the free surface of the melt, is usually coupled with buoyancy-driven flow. The influence of the thermocapillary convection is dominant in float-zone crystal growths, especially under microgravity conditions or in small-scale systems. Experiments on thermocapillary convection in a model of the float-zone process performed by Schwabe *et al.* [1], Chun [2], Kamotani *et al.* [3] and Preisser *et al.* [4] have shown that flow instability occurs when the Marangoni number, which governs the strength of the thermocapillary convection, is higher than the critical Marangoni number Ma_c, where Ma_c is strongly dependent on the aspect ratio of the melt and the properties of the fluid in that melt [5]. Jurisch and Löser [6] have demonstrated that the strictly periodic, non-rotational W striations, which are generated by the oscillatory thermocapillary convection, may appear in the single molybdenum (Mo) crystals.

When the length of the molten zone approaches a critical value the capillary instability originating from the gas–melt interface sets in, and the float zone may fall out. Both experimental and theoretical studies [7, 8] have shown that in a zero-gravity environment the maximum zone length of isothermal liquid bridges with rod radius R is equal to $2\pi R$ (Rayleigh limit). Coriell *et al.* [9], using the variational technique, showed that the maximum zone length decreases with an increase in the strength of the gravity compared with that of the surface-tension. Kim *et al.* [10] have measured the maximum stable zone lengths in a float-zone growth of small diameter sapphire and silicon. The results are in close agreement with the theoretical results. The computational results of Chen *et al.* [11] show that the maximum length of the non-isothermal liquid bridges is below the Rayleigh limit, and is affected by the strength of thermocapillary and buoyancy-driven convections, as well as the degree of surface-tension variation. In addition, the properties of a growth crystal may be influenced by the shape of the solid–melt interface during the growth. The experimental results of Kitamura *et al.* [12] have shown that screw dislocations tend towards the crystal edge when the growing interface is convex towards the melt, while the inclusions and the cracks are concentrated at the center of the crystal when the growing interface is concave towards the melt. In their opinion to grow a high quality single crystal the interface must be flat or convex towards the melt.

Since the quality of single crystals would be influenced by the flow state in the melt, the size of the melt, and the shape of solid–melt interface, it is important to predict the transport phenomena, both in the melt and in the solid, during the float-zone crystal growth process. Earlier researchers have studied the transport

NOMENCLATURE

Bi_c	convection Biot number
Bi_r	radiation Biot number
h	surface heat transfer coefficient
$i(r)$	dimensionless shape function of the solid–liquid interface
$i^*(r)$	shape function of the solid–liquid interface
k	thermal conductivity
l	length of the material rod
L	dimensionless length of the material rod
L_c	zone height at the centerline of the rod
l_p	width of the heated region
L_p	dimensionless heated width
L_s	zone height at the surface of the rod
Ma	Marangoni number
Pr	Prandtl number
P	dimensionless power
q	power density
Q	dimensionless power density
r	dimensionless radius coordinate
Re	Reynolds number
Rt	T_∞/T_m
r_0	radius of the material rod
T	temperature
T_m	melting temperature
T_∞	ambient temperature
u	dimensionless radial velocity
v	dimensionless axial velocity
z	dimensionless axial coordinate.

Greek symbols

α	thermal diffusivity
γ	surface-tension temperature coefficient
ε	emissivity
ζ	curvilinear coordinate.
η	curvilinear coordinate
Θ	dimensionless temperature
Θ_{max}	maximum temperature
μ	dynamic viscosity
ν	kinematic viscosity
σ	Stefan–Boltzmann constant
ψ	stream function
ω	vorticity.

Subscripts

l	liquid phase
n	normal derivative on the solid–melt interface
r, z	derivatives with respect to r, z
s	solid phase
ζ, η	derivatives with respect to ζ, η.

phenomena in float-zone crystal growth using some simple models. For example, Chang and Wilcox [13], Kobayashi [14], Fu and Ostrach [15] and Chen *et al.* [11] have all investigated the effect of thermocapillary flow in a model of a floating-zone crystal growth, without considering the effect of the solid–melt interface. Some investigators [16–19] have studied the influence of heat conduction on the float-zone growth. In general, those conduction analysis studies fall into two categories: specifying the ambient temperature distribution to predict the shape of molten zone, and finding the power requirement for producing a molten zone. They did not account for the effect of thermal convection. Recently, Lan and Kou [20–22] have investigated the interaction between the thermocapillary flow and the solid–melt interface in the float-zone crystal growth process. In their approach, the ambient temperature distribution is assumed to be known, and the pulling speed is selected as the characteristic velocity for the thermocapillary convection in the melt. In their results, the solid–melt interface is always concave towards the melt. In the real system, the ambient temperature distribution is unknown, and the power supplied by the external source is known. The results of Kobayashi [16] showed that the shape of the solid–melt interface is affected by the strength of the external power. Therefore, it is of interest to investigate the interaction between the thermocapillary convection and the zone shape for the different strength of the external power.

In the present paper we investigate the relationship between the power required for producing a molten zone and the zone shape through a series of numerical computations. The problem examined here is related to that of Kobayashi [16]. We go a step further by including the effect of thermocapillary convection. Buoyancy-driven convection is not taken into account. The influences of the heating conditions and the properties of the material on the flow fields, temperature fields, and the shape of the solid–melt interface are also investigated. In addition the possibility of the capillary instability originating from the gas–melt interface and convection instability in the melt is discussed.

2. MATHEMATICAL FORMULATION

Consider a long, circular rod of radius r_0 and length l which is heated by a ring heater at the center of the rod. The power distribution is assumed to be uniform with the heated width l_p and the density q. The molten zone is formed and is suspended between the solid ends. No crystal grows, and the input power used to melt a small portion of the material rod is dissipated from the rod surface by thermal convection and/or radiation. A schematic diagram of the system is shown

in Fig. 1. The melt from the rod contains an incompressible, Newtonian liquid. The gas–melt interface is assumed to have a large mean surface tension with no resulting surface deformation. The physical properties of the rod are assumed to be the same for both liquid and solid phases. The surface tension is considered as a linear decreasing function of temperature. The buoyancy effect is neglected.

We chose scales for length, velocity and pressure to be r_0, $(\gamma T_m)/\mu$ and $(\gamma T_m)/r_0$, respectively; μ is the viscosity of the melt, γ is the negative rate of change of surface tension with temperature, and T_m is the melting temperature. The dimensionless temperature is defined by $\Theta = (T-T_m)/T_m$. By eliminating the pressure, the dimensionless equations governing the steady, axisymmetic motion of the rod can be expressed in the following form:

(i) energy equation in the solid region

$$\Theta_{rr}+\frac{1}{r}\Theta_r+\Theta_{zz}=0 \tag{1a}$$

(ii) momentum equation in the melt

$$Re\left(-\frac{\omega}{r^2}\psi_z+\frac{1}{r}\psi_z\omega_r-\frac{1}{r}\psi_r\omega_z\right)$$

$$=\omega_{rr}+\frac{1}{r}\omega_r+\omega_{zz}-\frac{1}{r^2}\omega \tag{1b}$$

(iii) stream equation in the melt

$$\psi_{rr}-\frac{1}{r}\psi_r+\psi_{zz}=r\omega \tag{1c}$$

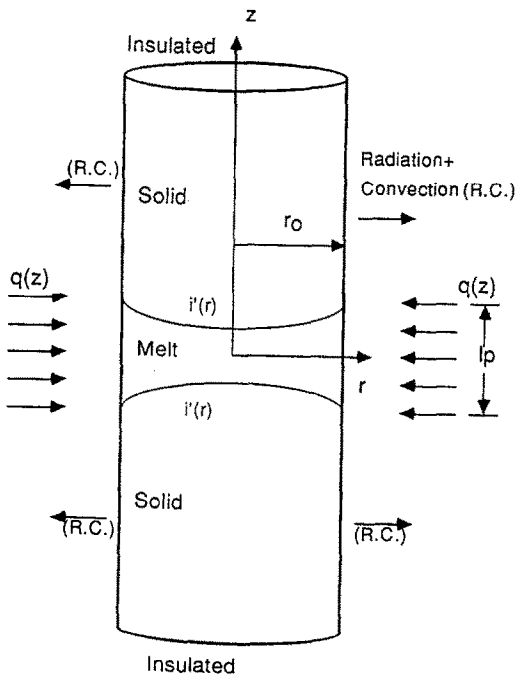

FIG. 1. Schematic diagram of the physical system.

(iv) energy equation in the melt

$$Pr\cdot Re\left(\frac{1}{r}\psi_z\Theta_r-\frac{1}{r}\psi_r\Theta_z\right)=\Theta_{rr}+\frac{1}{r}\Theta_r+\Theta_{zz}. \tag{1d}$$

Here, the streamfunction ψ in the r–z plane is given by

$$u=\frac{1}{r}\psi_z, \qquad v=-\frac{1}{r}\psi_r \tag{2a}$$

and the vorticity ω is defined as

$$\omega=u_z-v_r. \tag{2b}$$

The subscripts r and z denote the partial derivatives $\partial/\partial r$ and $\partial/\partial z$, respectively.

The dimensionless parameters appearing in governing equations are: $Pr=\nu/\alpha$ (Prandtl number) and $Re=\gamma T_m r_0/\mu\nu$ (Reynolds number), where α is the thermal diffusivity and ν is the kinematic viscosity.

The thermal boundary conditions are as follows:

(i) symmetry at the center line

$$\Theta_r=0 \quad \text{at } r=0 \tag{3a}$$

(ii) energy balance at the surface of the material rod

$$-\Theta_r=Bi_r[(\Theta+1)^4-Rt^4]+Bi_c(\Theta+1-Rt)-Q(z)$$

$$\text{at } r=1 \tag{3b}$$

(iii) temperature maintaining the melting point at the solid–melt interface

$$\Theta=0 \quad \text{at } z=i(r) \tag{3c}$$

(iv) energy balance at the solid–melt interface

$$(\Theta_n)_s=(\Theta_n)_l \quad \text{at } z=i(r) \tag{3d}$$

(v) no heat transfer far from the molten region

$$\Theta_z=0 \quad \text{at } z=L/2 \tag{3e}$$

(vi) temperature symmetric at the midplane

$$\Theta_z=0 \quad \text{at } z=0. \tag{3f}$$

The function $Q(z)$ is given by

$$Q(z)=\begin{cases}0, & \text{if } -\dfrac{L}{2}\leqslant z<-\dfrac{L_p}{2}, \quad \text{or} \dfrac{L_p}{2}<z\leqslant\dfrac{L}{2}\\ Q, & \text{if } -\dfrac{L_p}{2}\leqslant z\leqslant\dfrac{L_p}{2},\end{cases} \tag{3g}$$

where $Q=qr_0(kT_m)$ (the dimensionless power density), $L=l/r_0$, and $L_p=l_p/r_0$. The dimensionless power is defined by $P=2\pi l_p q/kT_m=2\pi L_p Q$. The subscript n denotes the partial derivative of normal direction on the solid–melt interface, while the subscripts s and l denote the solid and liquid phases, respectively. The parameter Rt is defined by $Rt=T_\infty/T_m$, where T_∞ is the ambient temperature. The appropriate fluid

flow boundary conditions in the molten region are as follows:

(i) symmetry at the centerline,

$$\psi = \omega = 0 \quad \text{at } r = 0 \tag{4a}$$

(ii) no normal velocity and shear stress balance at the free surface in the melt

$$\psi = 0 \tag{4b}$$

$$\omega = \Theta_z \quad \text{at } r = 1; \tag{4c}$$

(iii) no slip at the solid–melt interface

$$\psi = 0 \tag{4d}$$

$$\psi_{rr} - \frac{1}{r}\psi_r + \psi_{zz} = r\omega \quad \text{at } z = i(r), \tag{4e}$$

(iv) symmetry at the midplane

$$\psi = \omega = 0 \quad \text{at } z = 0. \tag{4f}$$

The boundary conditions contain the following dimensionless parameters: $Bi_r = \varepsilon\sigma T_\infty^3 r_0/k$ (Biot number of radiation) and $Bi_c = hr_0/k$ (Biot number of convection), where ε is the emissivity, σ is the Stefan–Boltzmann constant and h is the surface heat transfer coefficient.

3. SOLUTION PROCEDURE

In the present problem only a small portion of the rod near the heater is melted. The solid–melt interface is curved. Therefore, if the rectangular grid points are placed in the physical domain interpolation between grid points to represent boundary conditions at the solid–melt interface passing through a rectangular grid must be used. This results in a complex computer code. To avoid this difficulty a boundary-fitted curvilinear coordinate system developed by Thompson *et al.* [23] has been used to transfor the irregular physical domains (r, z) of the solid and liquid regions into two rectangular computational domains (ζ, η). The larger temperature and velocity gradients exist near the free surface and the solid–melt interface. The grid stretching, which provides good resolution near the free surface and solid–melt interface, is achieved by employing the grid control method developed by Middlecoff and Thomas [24].

The shape of solid–melt interface is unknown *a priori*, but must be determined as part of the overall solution. By assigning a specific shape to the solid–melt interface and temporarily discarding the Stefan condition (3d), a complete solution of the velocity and temperature fields can be determined from the governing equation (1) and boundary conditions (3) and (4). The Stefan condition then provides a means to examine whether the solid–melt interface shape is a required solution or not, and a basis for computing an improved estimate of that shape when the condition is not satisfied.

When a given estimated shape $z = i(r)$ for the solid–melt interface is incorrect, the heat flux on the interface cannot be balanced. The imbalance $\delta(r)$ can be written in the form

$$\delta(r) = \frac{1 + [i(r)_r]^2}{J}[(r_\eta\Theta_\zeta - r_\zeta\Theta_\eta)_\zeta - (r_\eta\Theta_\zeta - r_\zeta\Theta_\eta)_\eta], \tag{5}$$

where $J = r_\eta z_\zeta - r_\zeta z_\eta$ and the subscripts ζ and η denote the partial derivatives $\partial/\partial\zeta$ and $\partial/\partial\eta$, respectively. The imbalance $\delta(r)$ may not be to zero, due to an incorrect interface shape. We use $\delta(r)$ to correct the magnitude of the local displacement of the given interface, and the new shape $i(r)$ of the solid–melt interface is given by

$$i(r)^{\text{new}} = i(r)^{\text{old}} + \tau\delta(r), \tag{6}$$

where τ is a constant determined by numerical experiment with typical values being $O(10^{-3})$.

The discrete form of the system is constructed using standard second-order central differencing. A brief summary of this computational procedure involves the following steps. The solution of the difference equations begins with an initial shape of the solid–melt interface determined by solving the pure conduction equation. The initial guesses for Θ, ω and ψ over the entire computational domain are then selected. The liquid and solid regions are transferred to computational domains separately, using a boundary-fitted curvilinear coordinate system that has coordinate lines coincident with the current boundaries. The differential equations for ω and Θ are integrated by the predictor–corrector–multiple-iteration technique (PCMI). The PCMI method treats the ζ direction implicitly and the η direction explicitly. The ψ equation is solved iteratively using the LSOR method. The iteration process is assumed to converge when the relative error of two successive iterations is less than 10^{-5}. The new shape of the solid–melt interface is determined from equation (6). The whole procedure is repeated iteratively until $\delta(r) < 5 \times 10^{-2}$.

4. RESULTS AND DISCUSSION

The numerical calculations described in the previous section were performed in double-precision arithmetic on the National Central University IBM540 and HP730 workstations. The chosen computational domain in the z direction must be large enough to approximate the assumption of a long material rod. For most materials the melting point of the material rod is much higher than the ambient temperature ($Rt < 1$). Therefore, in the present study, the dimensionless length of the rod and the value of Rt are selected as $L = 20$ and $Rt = 0.2$, respectively. To determine the proper number of grid points, calculations were performed using different grid points. Table 1 shows the effect of grid distributions on the

Table 1. Effect of grid points on the solution for $Pr = 0.1$, $Re = 100$, $Bi_r = 0.1$, $Bi_c = 0$, $Rt = 0.2$, $P = 12.56$, and $L_p = 2$

NR, NZ_l, NZ_s	11, 31, 31	21, 31, 31	31, 31, 31	41, 41, 41	51, 51, 41
ψ_{max}	0.1385	0.1384	0.1381	0.1384	0.1383
Θ_{max}	0.6799	0.6806	0.6814	0.6822	0.6815
L_s	3.802	3.798	3.809	3.874	3.885
L_c	4.095	4.094	4.107	4.110	4.117

accuracy of the numerical solution for $Pr = 0.1$, $Re = 100$, $Bi_r = 0.1$, $Bi_c = 0$, $Rt = 0.2$, $P = 12.56$ and $L_p = 2$. In Table 1, L_c and L_s represent the zone height at the centerline and surface of the rod, respectively, while NR, NZ_l and NZ_s denote the grid points of r direction and z direction on the melt and solid regions, respectively. The results showed that the difference in the maximum stream function ψ_{max} and the maximum temperature Θ_{max}, L_c, and L_s calculated using different grids is less than 1%. To save computation time, the grid was selected as (31, 31, 31) for lower $Pr\ Re\ Q$. Due to the effect of the thermocapillary convection, the velocity and temperature gradients near the solid–melt interface increase as the magnitude of $Pr\ Re\ Q$ increases. Hence, the denser grid distribution is needed for higher $Pr\ Re\ Q$. The grid distribution selected by the present computation is (31, 31, 31), (41, 41, 41), (51, 51, 41), or (61, 61, 41), depending on the strength of $Pr\ Re\ Q$.

Figures 2 and 3 illustrate the influence of the input power on the solid–melt interface, the flow fields, and the temperature fields in the melt for two different values of Pr. In Figs. 2(a) and 3(a), the flow motion is counterclockwise because of the effect of the thermocapillary force. Figures 2 and 3 show that ψ_{max} increases as P increases, which means that the strength of the thermocapillary convection increases with the increase in input power. It is interesting to note that the Prandtl number, Pr, is defined as the ratio of momentum diffusivity to thermal diffusivity. For $Pr = 0.01$, the temperature field (Fig. 2b) is governed by conduction since the momentum diffusion is much less than the thermal diffusion. The energy transport in the heated region is mainly in the radial direction. Initially, the molten zone is formed on the surface in the heated region and the zone grows radially as well as axially with the increase of input power. When the molten zone without the core is formed the heat transport in the axial direction becomes significant and with further increase of the input power the growth rate of the molten zone near the center becomes faster than it is in the region near the gas–melt interface because of the radiation and convection loss on the surface. Hence, the present results for $Pr = 0.01$ (Fig. 2) show that the solid–melt interface varies from convex towards the melt, through flat to concave, when P increases. Obviously, these results are consistent with those of Kobayashi [16]. For $Pr = 10$ the influence of momentum diffusion becomes more significant with the increase of the input power. Therefore, the energy transfer in the axial direction is enhanced by the momentum transfer generated by the thermocapillary flow. Obviously, the energy transfer due to the momentum transfer in the region near the gas–melt interface is more than it near the center. This is why the results for $Pr = 10$ (Fig. 3) show that the solid–liquid interface is always convex towards the melt and the zone length is greater than it for $Pr = 0.01$ with the same input power. From Fig. 3(b), we see that the isothermal line is distorted more dramatically for higher P due to the increase of the strength of the thermocapillary convection.

Figures 4 and 5 demonstrate the effect of the Prandtl number for $Re = 1000$, $Bi_r = 0.1$, $Bi_c = 0$, $P = 5.66$ and $L_p = 2$. In Fig. 4, the results show that the molten zone enlarges, the absolute value of ψ_{max} increases, and the maximum temperature Θ_{max} decreases, when Pr increases. The isothermal line contour changes drastically as Pr increases. For $Pr = 10$, the isothermal line is distorted and most of the temperature variation occurs near the solid–melt interface and the heated region due to the effect of the thermocapillary convection. The increase of the molten zone for higher Pr is caused by the effect of the thermocapillary convection which increases the heat transport in the axial direction. For $Pr = 0.01$, the surface temperature shows a Gaussian distribution (Fig. 5) which is similar to that obtained by the conduction model with uniform input power calculated by Carlberg and Levenstam [19]. It is obvious that, given fixed other parameters, the surface temperature gradient along near the heat source decreases when Pr increases. But, the surface temperature gradient near the solid–melt interface gets larger for higher Pr.

Figure 6 shows the effect of the input power on the zone heights for $Re = 1000$, $Bi_r = 0.1$, $Bi_c = 0$, and $L_p = 2$ with two different Pr. When $L_c < L_s$, the solid–melt interface is convex towards the melt. On the other hand, the solid–melt interface is concave for $L_c > L_s$. When $L_c < L_s$, the solid–melt interface is flat. For $Pr = 0.01$ and $P = 3.9$, the results show $L_c = L_s \approx L_p$. This is consistent with results obtained by Kobayashi [16]. For $Pr = 10$, the solid–melt interface is always convex towards the melt ($L_c < L_s$). From Fig. 6, we can see that the growth rate of the molten zone for $Pr = 10$ is much faster than for $Pr = 0.01$ when P increases. For $Pr = 0.01$, the zone heights increase steeply until $L_s = L_c$, and then increase gradually with the increase in input power. On the contrary, for $Pr = 10$, the zone heights always increase steeply.

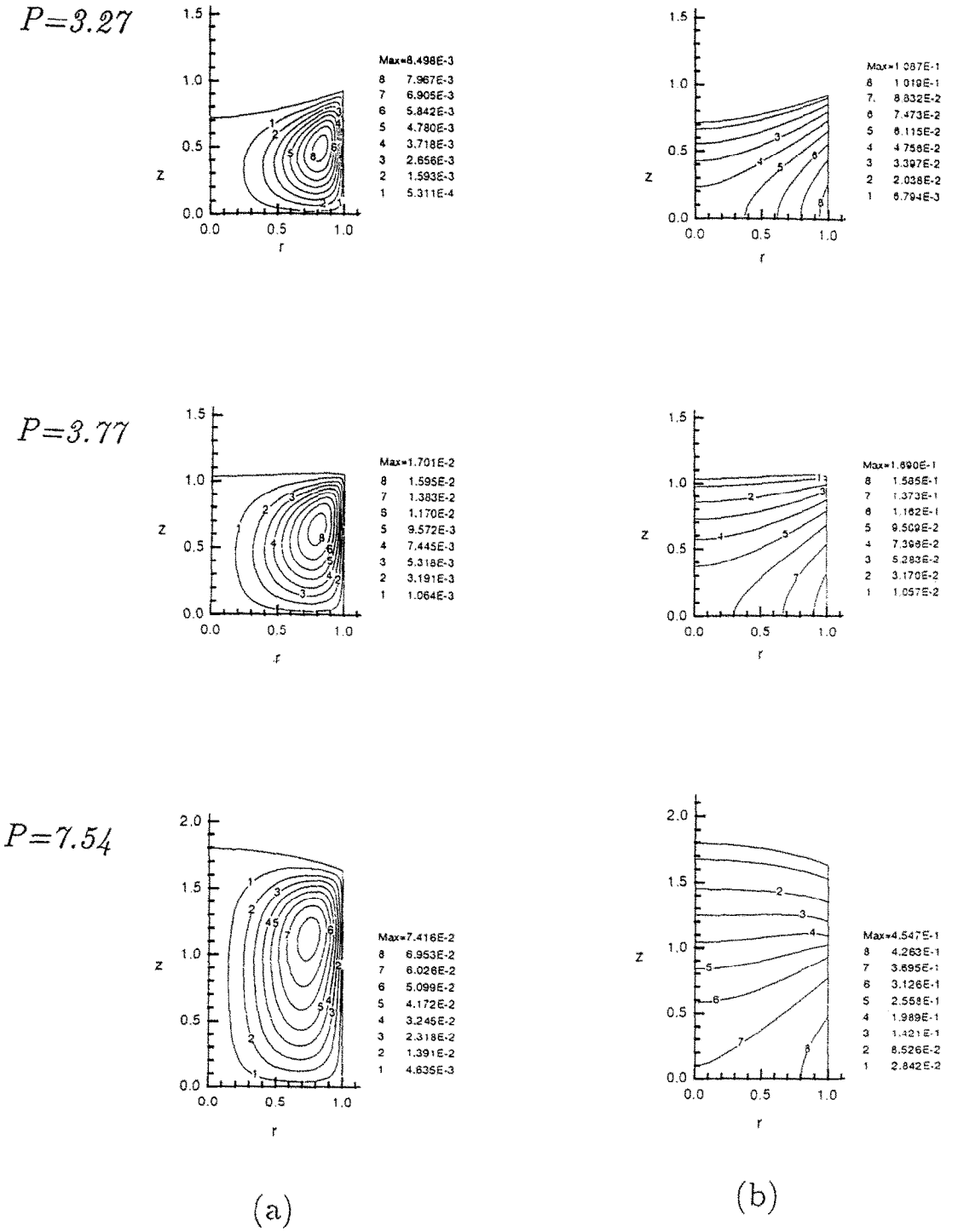

FIG. 2. Contours for (a) streamlines and (b) isothermals in the melt for $Pr = 0.01$, $Re = 1000$, $Bi_c = 0$, $Bi_r = 0.1$, and $L_p = 4$ with three different P.

Based on the results of the capillary instability, the maximum zone length is restricted by the Rayleigh limit ($L_s = 2\pi$). For $L_s \geqslant 2\pi$, capillary instability sets in and the molten zone may break up. It is clear that the power requirement for forming a molten zone with $L_s = 2\pi$ for $Pr = 10$ is much smaller than it is for $Pr = 0.01$. This suggests that the maximum input power for high Prandtl number materials is smaller than for small Prandtl number materials. It is possible that the capillary instability for small Prandtl number materials never occurs because the zone height is always less than the Rayleigh limit no matter how large the input power is. Since the present approach does not consider the effect of surface deformation of

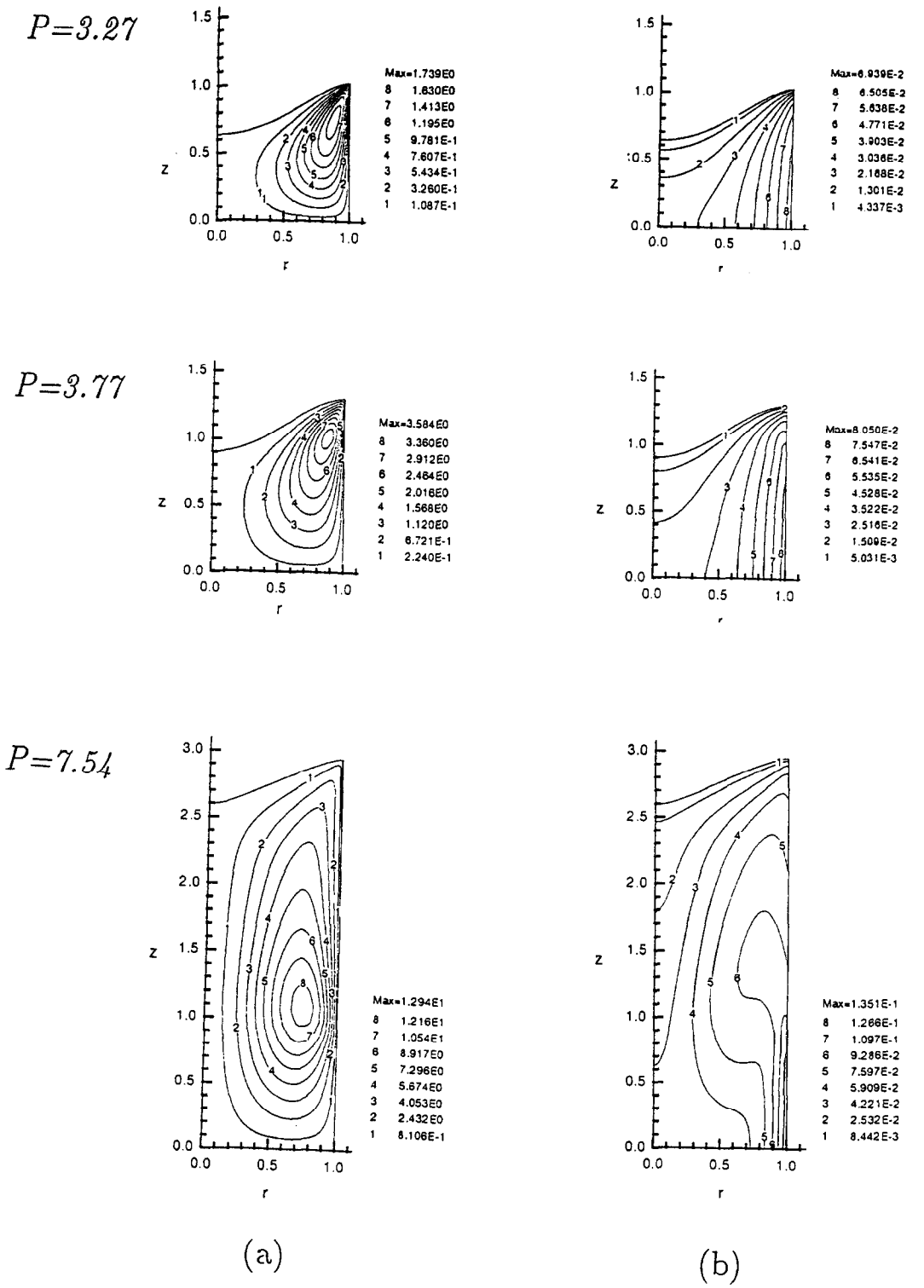

FIG. 3. Contours for (a) streamlines and (b) isothermals in the melt for $Pr = 10$, $Re = 1000$, $Bi_c = 0$, $Bi_r = 0.1$, and $L_p = 4$ with three different P.

the gas–liquid interface the convergent solutions are still possible when the zone height exceeds the Rayleigh limit.

The Reynolds number, Re, represents the ratio of the surface tension to the viscous force. The magnitude of the Reynolds number is independent of the heating condition and is strongly influenced by the property of the melt and the geometry of the rod. Its order is around 10^2 to 10^4 for most oxide materials, and over 10^4 for semiconductor materials. Figure 7

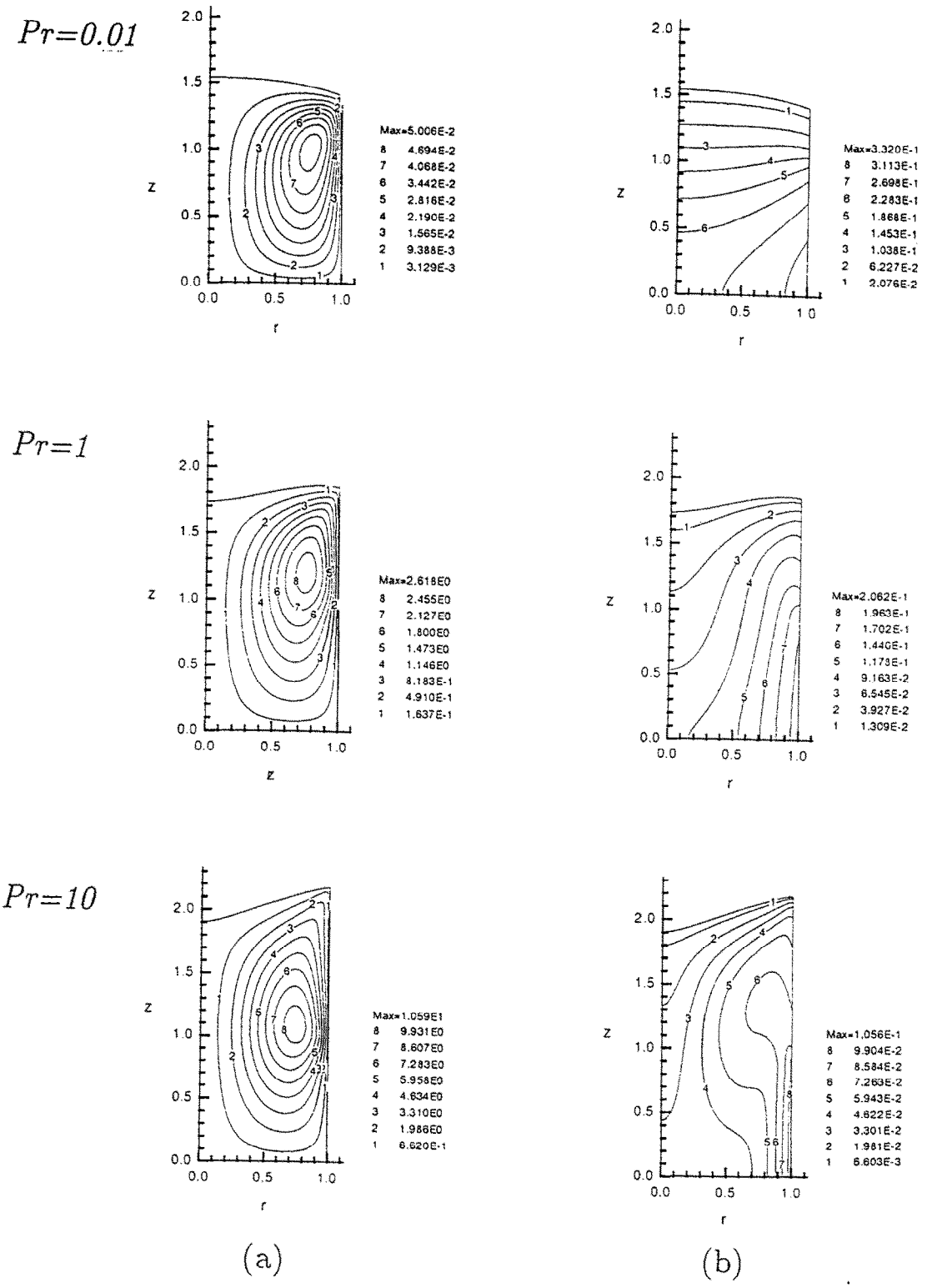

FIG. 4. Contours for (a) streamlines and (b) isothermals in the melt for $Re = 1000$, $Bi_c = 0$, $Bi_r = 0.1$, $L_p = 2$, and $P = 5.66$ with three different Pr.

displays the influence of Re for $Pr = 10$, $Bi_r = 0.1$, $Bi_c = 0$, $p = 5.655$, and $L_p = 2$. In Fig. 7 the results show that with other parameters fixed Ψ_{max} gets larger and the isothermal line is more significantly distorted for higher Re. It is clear that the strength of the thermocapillary convection increases with increasing Re. Because the input heat is maintained at a constant value Θ_{max} decreases with increasing Re due to the

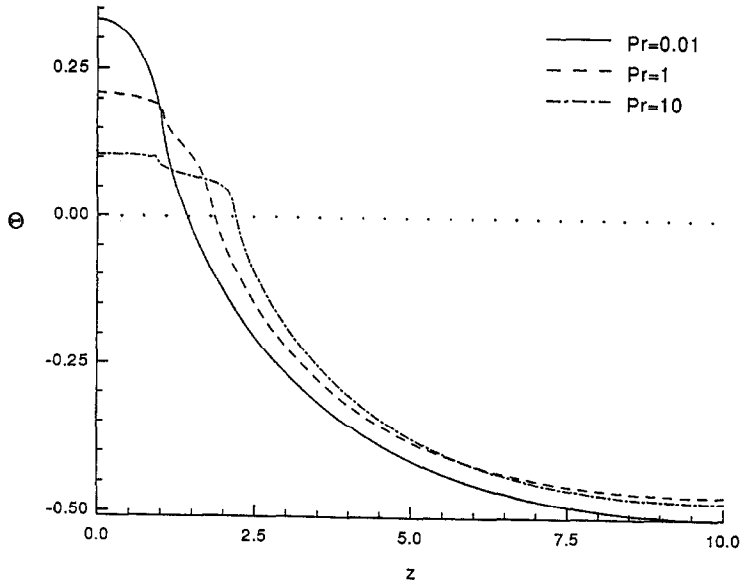

FIG. 5. Variation of the surface temperature for $Re = 1000$, $Bi_c = 0$, $Bi_r = 0.1$, $L_p = 2$, and $P = 5.66$ with three different Pr.

stronger thermocapillary convection. The zone shape and height is almost invariant with the change of the Reynolds number.

Figure 8 shows the influence of the width of the heated region L_p. In Fig. 8(a), the present results for $Pr = 0.01$ are consistent with those of Kobayashi [16] in that the powers required to form the molten zone and for $L_s = L_c$ are strongly dependent on L_p. In Fig. 8(b) the results show that for $Pr = 0.01$ and 10, the zone height of $L_p = 4$ is less than that of $L_p = 2$ for smaller input power, and then becomes larger than that of $L_p = 2$ for higher input power. The trends for $Pr = 0.01$ are similar to that obtained by the conduction analysis [19]. The radiation Biot number, Bi_r, represents the ratio of the surface radiation to the conduction inside the rod. Figure 9 shows the influence of Bi_r on the zone heights of the rod. The minimum power required to form a molten zone for $Bi_r = 0.05$ is smaller than that for $Bi_r = 0.1$ because the net heat input the rod increases with the decrease of Bi_r. The effect of the convection Biot number, Bi_c, is also investigated. They show similar trends as the influence of the radiation Biot number.

Following Velten *et al.* [5], the Marangoni number can be defined by

$$Ma = 2Pr\,Re\,\Theta_{\max}/L_s.$$

This is usually used to represent the strength of the

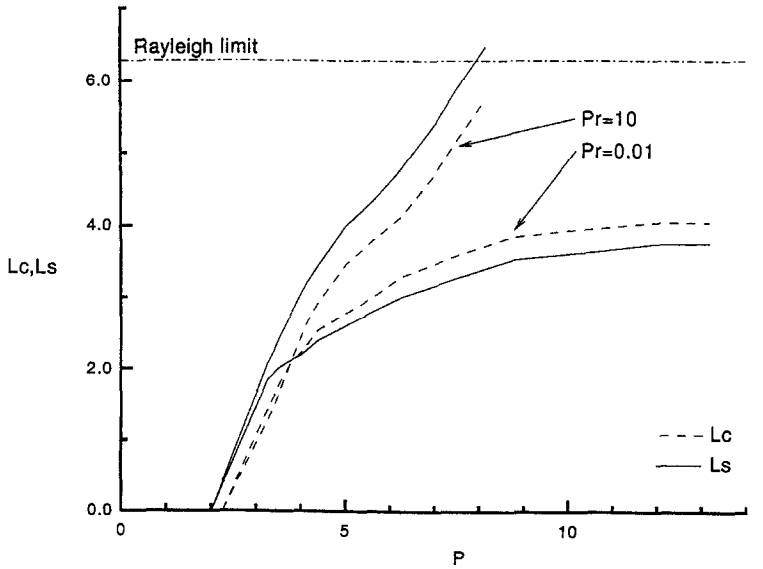

FIG. 6. Zone heights vs input power P and Pr for $Re = 1000$, $Bi_c = 0$, $Bi_r = 0.1$, and $L_p = 2$.

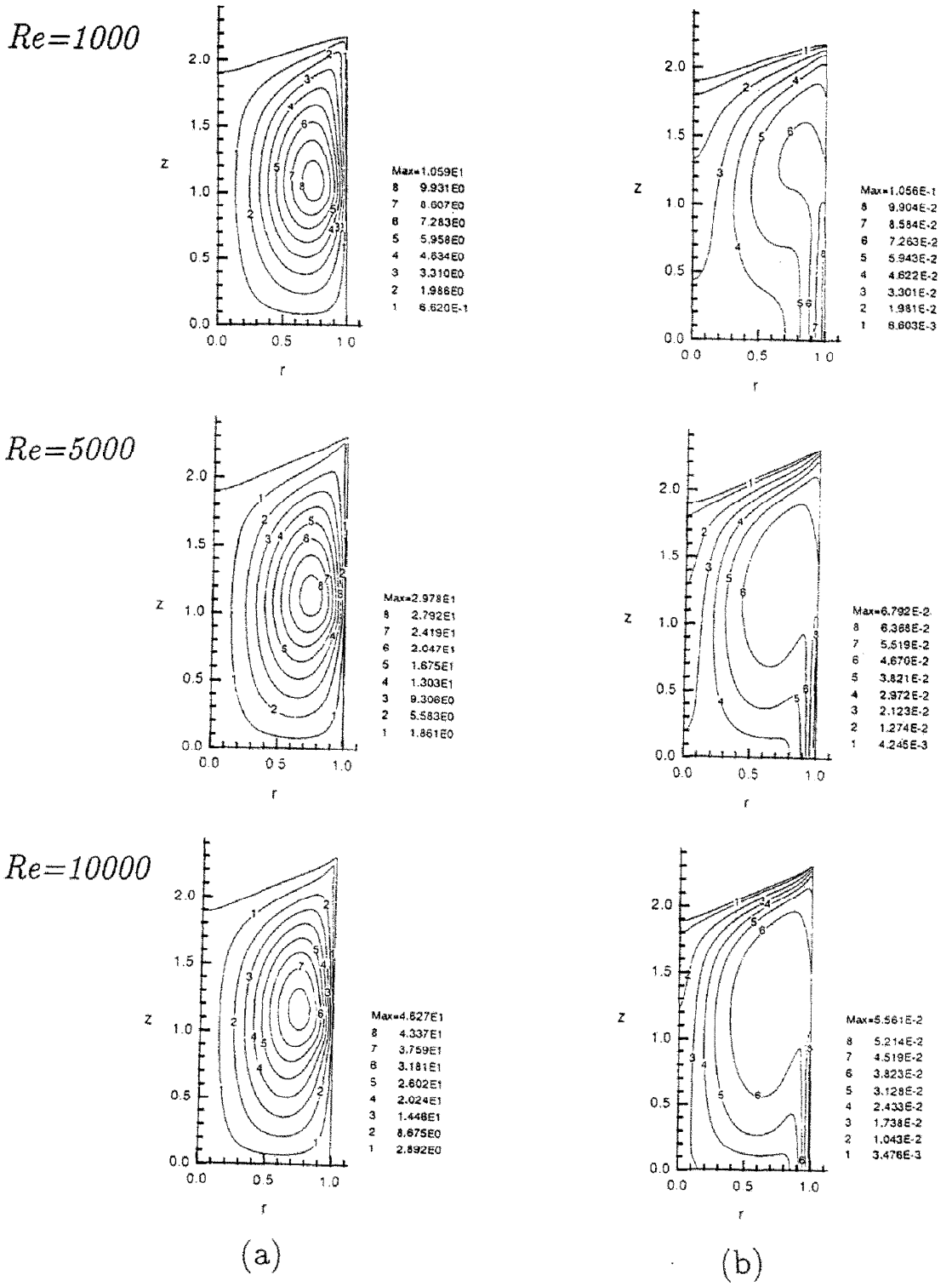

FIG. 7. Contours for (a) streamlines and (b) isothermals in the melt for $Pr = 10$, $Bi_c = 0$, $Bi_r = 0.1$, $L_p = 2$, and $P = 5.66$ with three different Re.

thermocapillary convection. Figure 10 shows the influence of the input power on the Marangoni number and Θ_{max} for $Re = 1000$, $Bi_r = 0.1$, $Bi_c = 0$, and $L_p = 2$ with two different Pr. The maximum temperature Θ_{max} also represents the temperature difference along the gas–melt interface and it increases as P increases. The increase rate of Θ_{max} for $Pr = 0.01$ is much higher than for $Pr = 10$, and the magnitude of Θ_{max} for $Pr = 0.01$ is always larger than for $Pr = 10$. On the contrary, the growth rate of the zone height

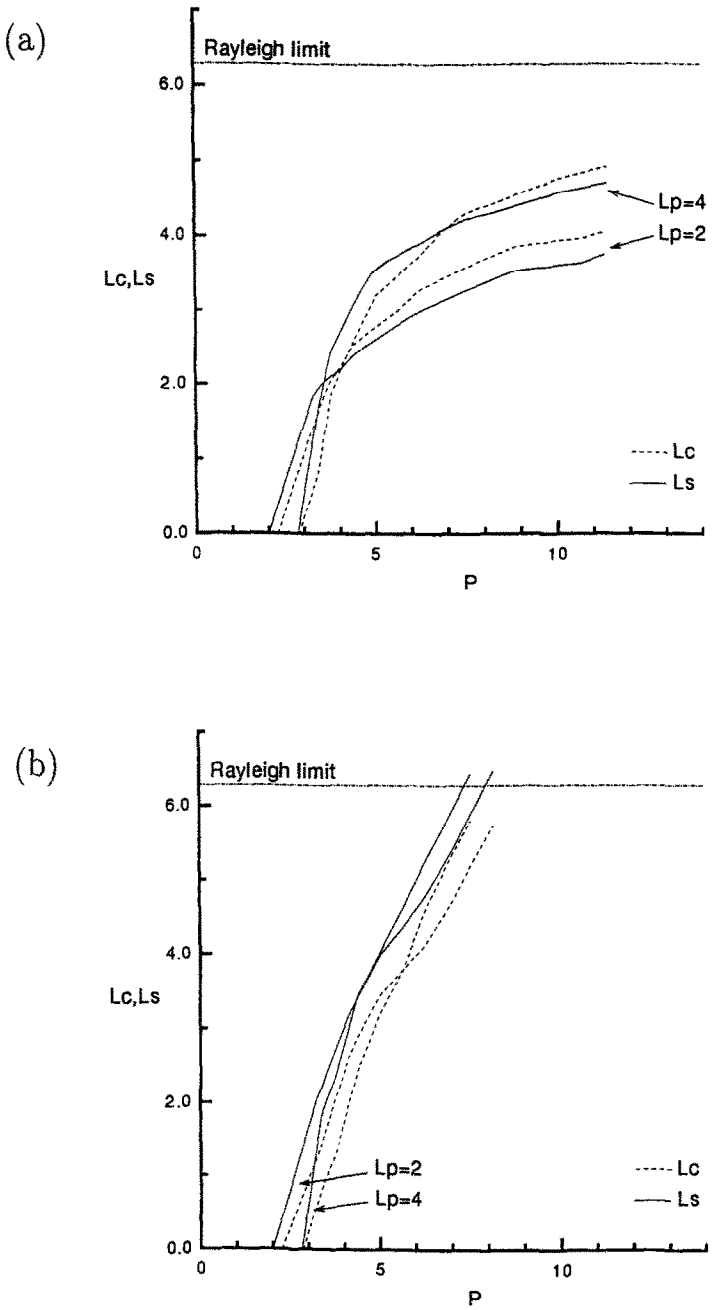

FIG. 8. Zone heights vs input power P and width of the heated region L_p for $Re = 1000$, $Bi_c = 0$, and $Bi_r = 0.1$ with (a) $Pr = 0.01$ and (b) $Pr = 10$.

for $Pr = 10$ is much faster than for $Pr = 0.01$ (Fig. 6). Figure 10 shows the expected results that the Marangoni number increases with increasing of P for $Pr = 0.01$, and it decreases with increasing of P for $Pr = 10$ when $P > 3.5$. Figure 11 illustrates the variation of the Marangoni number with the surface zone height L_s. For smaller Pr, the heat transfer is dominated by conduction in the radial direction. When the input power increases, the increase in the temperature difference along the gas–melt interface is higher than that of L_s. This is why the Marangoni number increases with the increase of L_s for $Pr = 0.01$. The Marangoni number increases abruptly as $L_s/2 > 1.9$, since L_s increases slowly as P increases (Fig. 6). For $Pr = 10$, the heat transfer in the axial direction is enhanced by the effect of the thermocapillary convection. In Fig. 11, the Marangoni number for $Pr = 10$ increases with increasing $L_s/2$ until $L_s/2$ reaches a certain value: $L_m/2$, which is very close to the value of $L_p/2$. For $L_s/2 > L_m/2$, the Marangoni number decreases as $L_s/2$ increases. As $L_s/2 < L_m/2$, the convection effect is still insignificant and the heat transfer is mainly in the radial direction. Therefore, the Marangoni number increases slightly with the increase of

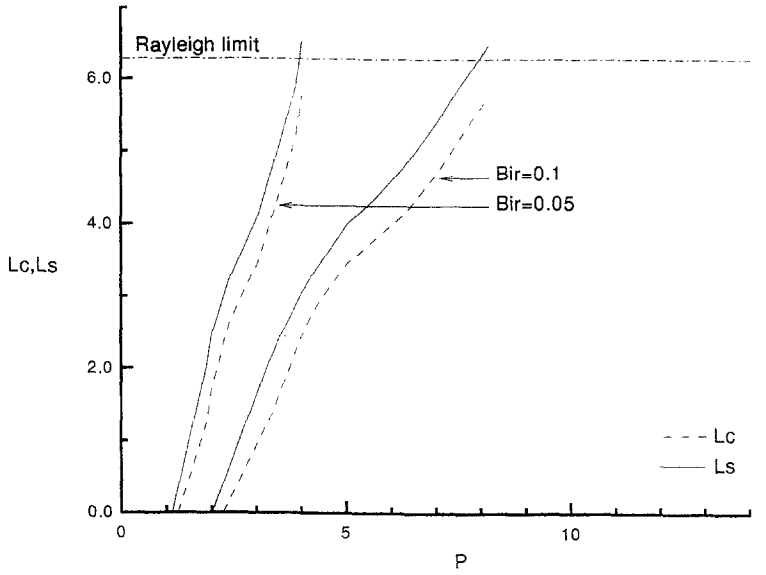

FIG. 9. Zone heights vs input power P and Bi_r for $Pr = 10$, $Re = 1000$, $Bi_c = 0$, and $L_p = 2$.

$L_s/2$. For $L_s/2 > L_m/2$, the thermocapillary convection becomes dominant and the increase in the temperature difference along the gas–melt interface is less than it is for L_s with the increase in input power. Hence, the Marangoni number decreases with the increase of $L_s/2$. According to the experimental results of the half-zone model [1–5], the flow instability is occurring in the presence of the stronger thermocapillary convection (higher Marangoni number). The magnitude of the critical Marangoni number is about $O(10^4)$, and decreases strongly as Pr decreases. Based on our results, we can conjecture that the possibility of the occurrence of thermocapillary-convection instability in the melt for $Pr = 0.01$ is higher than it is for $Pr = 10$.

Figures 12–14 show the influence of Re, L_p, and Bi_r on Ma. In Fig. 12, the results show that the magnitude of Ma is strongly dependent on the order of Re and, as one would certainly expect, increases with increasing Re. The trend of the variation of Ma with L_s is similar for two different Re. Obviously, for fluids with higher Re the instability caused by the thermocapillary convection may appear before the capillary instability sets in. On the contrary, for fluids with smaller Re the thermocapillary-convection instability never occurs.

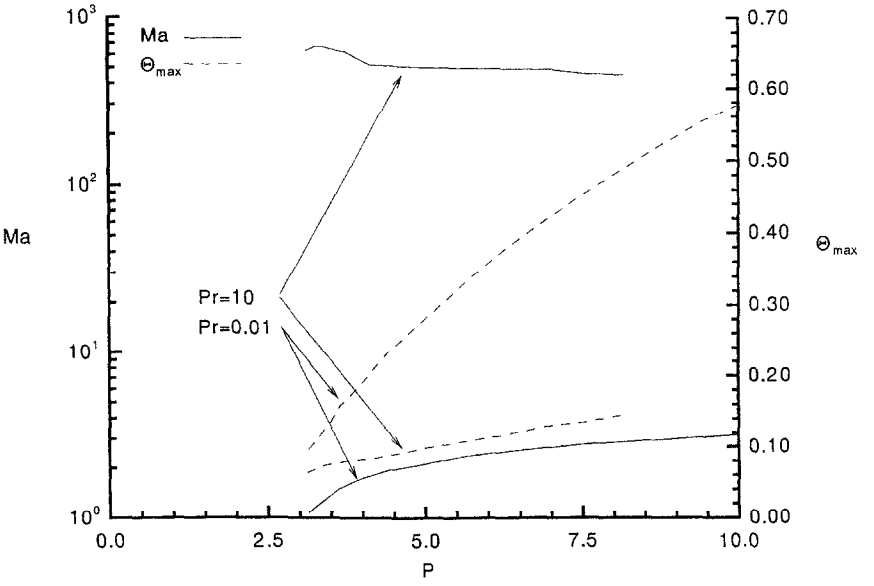

FIG. 10. Marangoni number and maximum temperature Θ_{max} vs input power P and Pr for $Re = 1000$, $Bi_c = 0$, $Bi_r = 0.1$, and $L_p = 2$.

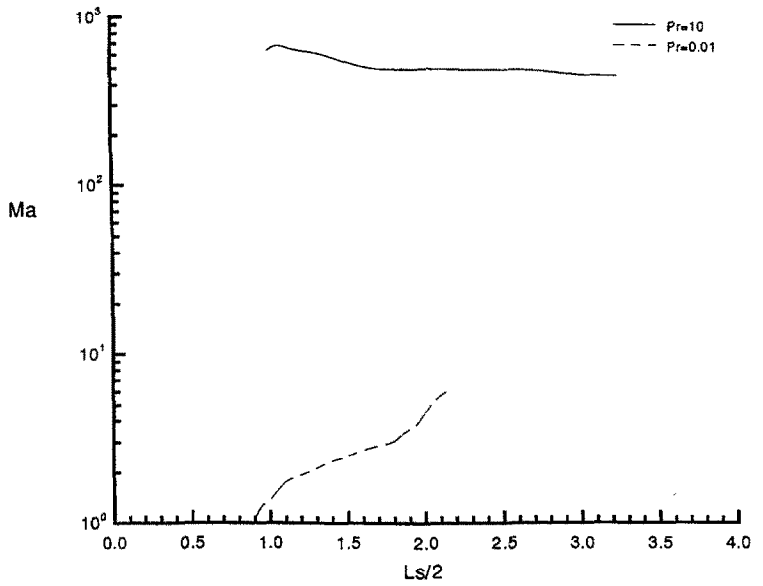

FIG. 11. Marangoni number vs surface zone height L_s and Pr for $Re = 1000$, $Bi_c = 0$, $Bi_r = 0.1$, and $L_p = 2$.

Figure 13 illustrates that the magnitude of Ma for $L_p = 2$ is higher than for $L_p = 4$. For $Pr = 10$, the variation of Ma with L_s still shows a similar trend, in that Ma increases with increasing L_s for $L_s < L_m$, and decreases with increasing L_s for $L_s < L_m$. It is obvious that the order of the Marangoni number is strongly influenced by the heating conditions. With a fixed zone height the temperature gradient along the gas–melt interface is higher for a larger input power. The power required to reach a certain value of L_s increases as Bi_r increases (Fig. 9). This is the reason that in Fig. 14 the Marangoni number increases with the increase of the radiation loss. The effect of the convection Biot number, Bi_c, on Ma is similar to that of the radiation Biot number. Therefore, the better heat transfer along the surface of the material rod will increase the magnitude of the Marangoni number.

5. CONCLUSIONS

It is well known that the quality of single crystals is influenced by the shape of the solid–melt interface and the thermocapillary-convection instability in the melt, while the size of the melt is controlled by the capillary instability originating at the gas–melt interface. Based on the opinions of Kitamura *et al.* [12] the solid–

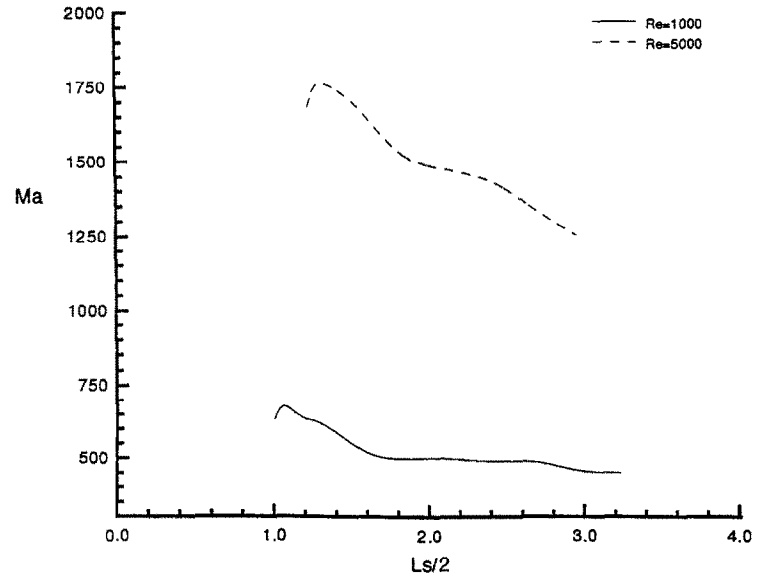

FIG. 12. Marangoni number vs surface zone height L_s and Re for $Pr = 10$, $Bi_c = 0$, $Bi_r = 0.1$, and $L_p = 2$.

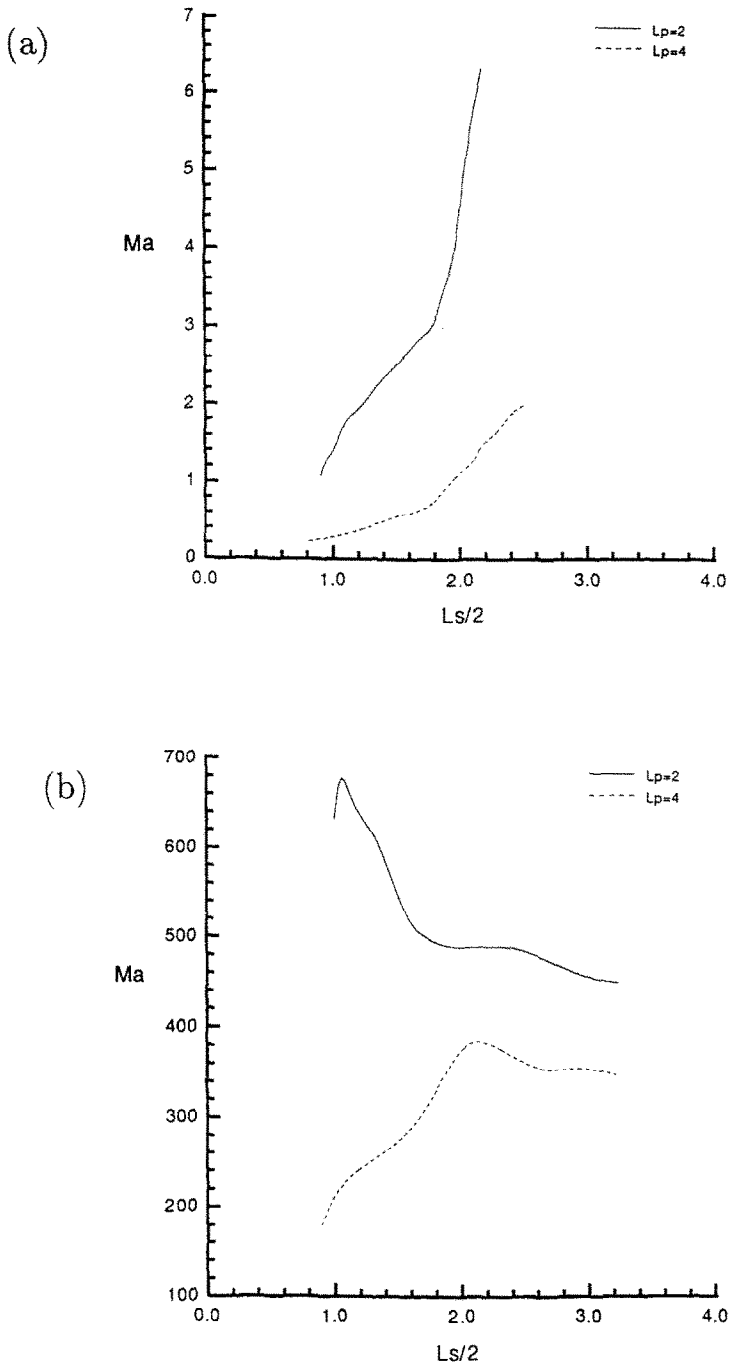

FIG. 13. Marangoni number vs surface zone height L_s and width of the heated region L_p for $Re = 1000$, $Bi_c = 0$, and $Bi_r = 0.1$ with (a) $Pr = 0.01$ and (b) $Pr = 10$.

melt interface should be maintained as flat or convex towards the melt, to grow high quality single crystals. The present results show that the shape of the solid–melt interface is affected by the input power, the width of heated region, the Prandtl number, the radiation Biot number and the convection Biot number. For $Pr = 0.01$, to keep the solid–melt interface flat or convex towards the melt, the input power should be maintained at the lowest level practical. For $Pr = 10$, the solid–melt interface is always convex towards the melt. For a fixed input power, the strength of the thermocapillary convection is enhanced by the increase of the Prandtl and Reynolds numbers, and by the decrease in the width of the heated region, radiation, and convection loss.

Thermocapillary convection enhances the heat transfer in the axial direction, then enlarges the length of the molten zone. Hence, the maximum input power to produce a melt with a zone height less than the Rayleigh limit is reduced by increasing the effect of

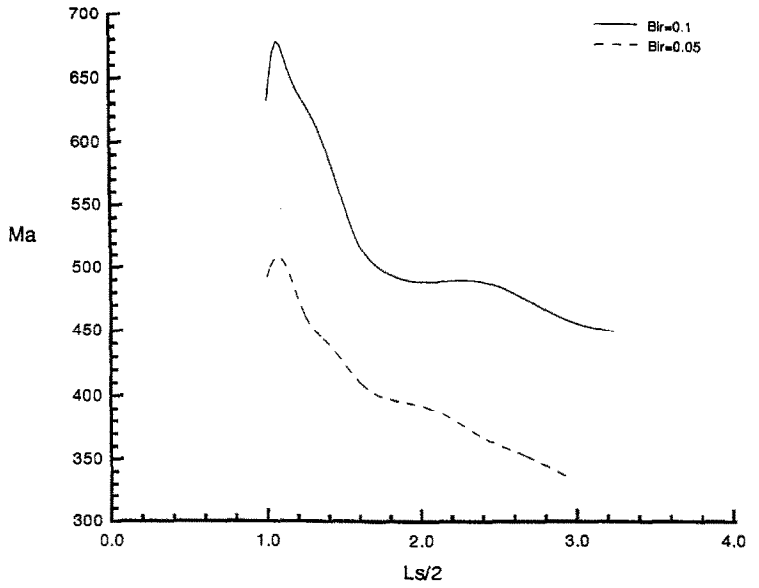

FIG. 14. Marangoni number vs surface zone height L_s and Bi_r for $Pr = 10$, $Re = 1000$, $Bi_c = 0$, and $L_p = 2$.

thermocapillary convection. For small Prandtl number fluids, the zone height increases steeply for $L_s > L_c$ when the input power increases, and it then increases slowly for $L_s < L_c$ with further increases in the input power. The possible zone length is always less than the Rayleigh limit which means that capillary instability will never occur. But, the thermocapillary-flow instability may set in, because the temperature gradient along the gas–liquid interface continuously increases. On the other hand, the zone height for high Prandtl number fluids continuously increases as the input power increases. Therefore, the possibility of the occurrence of capillary instability for high Prandtl number fluids is much higher than it for small Prandtl number fluids. For higher Prandtl number fluids, flow instability may set in with larger Re, smaller widths of the heated region, or larger heat loss to the ambient.

Acknowledgement—The authors gratefully acknowledge the support of the National Science Council of the R.O.C. for this work through grant No. NSC82-0401-E008-066.

REFERENCES

1. D. Schwabe, A. Scharmann, F. Preisser and R. Oeder, Experiments on surface tension driven flow in floating zone melting. *J. Crystal Growth* **43**, 305–312 (1978).
2. C.-H. Chun, Experiments on steady and oscillatory temperature distribution in a floating zone due to the Marangoni convection. *Acta Astronautica* **7**, 479–488 (1980).
3. Y. Kamotani, S. Ostrach and M. Vargas, Oscillatory thermocapillary convection in a simulated floating-zone configuration. *J. Crystal Growth* **66**, 83–90 (1984).
4. F. Preisser, D. Schwabe and A. Scharmann, Steady and oscillatory thermocapillary convection in liquid columns with free cylindrical surface. *J. Fluid Mech.* **126**, 545–567 (1983).
5. R. Velten, D. Schwabe and A. Scharmann, The periodic instability of thermocapillary convection in cylindrical liquid bridges. *Phys. Fluids A* **3**, 267–279 (1991).
6. M. Jurisch and W. Löser, Analysis of periodic non-rotational W striations in Mo single crystals due to non-steady thermocapillary convection. *J. Crystal Growth* **102**, 214–222 (1990).
7. W. G. Pfann and D. W. Hagelberger, Electromagnetic suspension of a molten zone. *J. Appl. Phys.* **27**, 12–18 (1965).
8. G. Mason, An experimental determination of the stable length of cylindrical liquid bubbles. *J. Colloid Interface Sci.* **32**, 172–176 (1970).
9. S. R. Coriell, S. C. Hardy and M. R. Coprdes, Stability of liquid zones. *J. Colloid Interface Sci.* **60**, 126–136 (1977).
10. K. M. Kim, A. B. Dreeben and A. Schujko, Maximum stable zone length in float-zone growth of small diameter sapphire and silicon crystals. *J. Appl. Phys.* **50**, 4472–4474 (1979).
11. J.-C. Chen, J.-C Sheu and Y.-T. Lee, Maximum stable length of nonisothermal liquid bridges. *Phys. Fluids A* **2**, 1118–1123 (1990).
12. K. Kitamura, S. Kimura and S. Hosoya, The interface shapes of some oxide materials grown by the floating zone method. *J. Crystal Growth* **48**, 469–472 (1980).
13. C. E. Chang and W. R. Wilcox, Analysis of surface tension driven flow in floating zone melting. *Int. J. Heat Mass Transfer* **19**, 335–366 (1976).
14. N. Kobayashi, Computer simulation of the steady flow in a cylindrical floating zone under low gravity. *J. Crystal Growth* **66**, 63–72 (1984).
15. B. Fu and S. Ostrach, Numerical solution of thermocapillary flows in floating zones. In *Transport Phenomena in Materials Processing*. ASME, New York (1985).
16. N. Kobayashi, Power required to form a floating zone and the zone shape. *J. Crystal Growth* **43**, 417–424 (1978).
17. Y. T. Chan, S. K. Choi and H. L. Grubin, A heat transfer study of float zone TiC growth. ASME paper 91-HT-42 (1991).
18. J. L. Duranceau and R. A. Brown, Thermal-capillary analysis of small-scale floating zones: steady-state calculation. *J. Crystal Growth* **75**, 367–389 (1986).

19. T. Carlberg and M. Levenstam, Laser-heating applied to microgravity experiments—a feasibility study. *Microgravity Sci. Technol.* **4,** 254–261 (1991).
20. C. W. Lan and Sindo Kuo, Thermocapillary flow and melt/solid interfaces in floating-zone crystal growth under microgravity. *J. Crystal Growth* **102,** 1043–1058 (1990).
21. C. W. Lan and Sindo Kuo, Heat transfer, fluid flow and interface shapes in floating-zone crystal growth. *J. Crystal Growth* **108,** 351–366 (1991).
22. C. W. Lan and Sindo Kuo, Effects of rotation on heat transfer, fluid flow and interfaces in normal gravity floating-zone crystal growth. *J. Crystal Growth* **114,** 517–535 (1991).
23. J. F. Thompson, F. C. Thames and W. Mastin, Automatic numerical generation of body fitted curvilinear coordinate system for field containing any number of arbitrary two-dimensional bodies. *J. Comput. Phys.* **15,** 299–319 (1974).
24. J. F. Middlecoff and P. D. Thomas, Direct control of the grid point distribution in meshes generated by elliptic equations. *AIAA J.* **18,** 652–656 (1980).